The Astrophysical Journal, 765:91 (8pp), 2013 March 10 doi:10.1088/0004-637X/765/2/91

TIME DEPENDENCE OF THE PROTON FLUX MEASURED BY PAMELA DURING THE 2006 JULY–2009 DECEMBER SOLAR MINIMUM

O. Adriani[1,2], G. C. Barbarino[3,4], G. A. Bazilevskaya[5], R. Bellotti[6,7], M. Boezio[8], E. A. Bogomolov[9], M. Bongi[1,2], V. Bonvicini[8], S. Borisov[10,11,12], S. Bottai[2], A. Bruno[6,7], F. Cafagna[7], D. Campana[4], R. Carbone[8], P. Carlson[13], M. Casolino[11], G. Castellini[14], M. P. De Pascale[10,11,21], C. De Santis[10,11], N. De Simone[10], V. Di Felice[10], V. Formato[8,15], A. M. Galper[12], L. Grishantseva[12], A. V. Karelin[12], S. V. Koldashov[12], S. Koldobskiy[12], S. Y. Krutkov[9], A. N. Kvashnin[5], A. Leonov[12], V. Malakhov[12], L. Marcelli[11], A. G. Mayorov[12], W. Menn[16], V. V. Mikhailov[12], E. Mocchiutti[8], A. Monaco[6,7], N. Mori[2], N. Nikonov[9,10,11], G. Osteria[4], F. Palma[10,11], P. Papini[2], M. Pearce[13], P. Picozza[10,11], C. Pizzolotto[8,17,18], M. Ricci[19], S. B. Ricciarini[14], L. Rossetto[13], R. Sarkar[8], M. Simon[16], R. Sparvoli[10,11], P. Spillantini[1,2], Y. I. Stozhkov[5], A. Vacchi[8], E. Vannuccini[2], G. Vasilyev[9], S. A. Voronov[12], Y. T. Yurkin[12], J. Wu[13,22], G. Zampa[8], N. Zampa[8], V. G. Zverev[12], M. S. Potgieter[20], and E. E. Vos[20]

[1] Department of Physics, University of Florence, I-50019 Sesto Fiorentino, Florence, Italy
[2] INFN, Sezione di Florence, I-50019 Sesto Fiorentino, Florence, Italy
[3] Department of Physics, University of Naples "Federico II," I-80126 Naples, Italy
[4] INFN, Sezione di Naples, I-80126 Naples, Italy
[5] Lebedev Physical Institute, RU-119991 Moscow, Russia
[6] Department of Physics, University of Bari, I-70126 Bari, Italy
[7] INFN, Sezione di Bari, I-70126 Bari, Italy
[8] INFN, Sezione di Trieste, I-34149 Trieste, Italy
[9] Ioffe Physical Technical Institute, RU-194021 St. Petersburg, Russia
[10] INFN, Sezione di Rome "Tor Vergata," I-00133 Rome, Italy
[11] Department of Physics, University of Rome "Tor Vergata," I-00133 Rome, Italy
[12] Moscow Engineering and Physics Institute, RU-11540 Moscow, Russia
[13] KTH, Department of Physics, and the Oskar Klein Centre for Cosmoparticle Physics, AlbaNova University Centre, SE-10691 Stockholm, Sweden
[14] IFAC, I-50019 Sesto Fiorentino, Florence, Italy
[15] Department of Physics, University of Trieste, I-34147 Trieste, Italy
[16] Department of Physics, Universität Siegen, D-57068 Siegen, Germany
[17] INFN, Sezione di Perugia, I-06123 Perugia, Italy
[18] Agenzia Spaziale Italiana (ASI) Science Data Center, I-00044 Frascati, Italy
[19] INFN, Laboratori Nazionali di Frascati, Via Enrico Fermi 40, I-00044 Frascati, Italy
[20] Centre for Space Research, North-West University, 2520 Potchefstroom, South Africa
Received 2012 October 31; accepted 2013 January 16; published 2013 February 20

ABSTRACT

The energy spectra of galactic cosmic rays carry fundamental information regarding their origin and propagation. These spectra, when measured near Earth, are significantly affected by the solar magnetic field. A comprehensive description of the cosmic radiation must therefore include the transport and modulation of cosmic rays inside the heliosphere. During the end of the last decade, the Sun underwent a peculiarly long quiet phase well suited to study modulation processes. In this paper we present proton spectra measured from 2006 July to 2009 December by PAMELA. The large collected statistics of protons allowed the time variation to be followed on a nearly monthly basis down to 400 MV. Data are compared with a state-of-the-art three-dimensional model of solar modulation.

Key words: cosmic rays – solar wind – Sun: heliosphere

Online-only material: color figures

1. INTRODUCTION

Protons are the most abundant species in cosmic rays, representing about 90% of the total flux. They are believed to be mainly of primordial origin, accelerated during supernovae explosions and confined within our Galaxy, at least up to PeV energies. During propagation through the interstellar medium, cosmic rays undergo interactions with gas atoms and lose energy significantly modifying their injection spectra and composition.

Besides the effect of propagation in the Galaxy, cosmic-ray particles reaching the Earth are affected by the solar wind and the solar magnetic field. A continuous flow of plasma emanates from the solar corona and extends out far beyond Pluto, up to the heliopause where the interstellar medium is encountered. The solar wind travels at supersonic speeds of about 350–650 km s^{-1} up to the termination shock where it slows down to about 100–150 km s^{-1} to form the inner heliosheath.

The plasma carries the solar magnetic field out into the heliosphere to form the heliospheric magnetic field (HMF). When interstellar cosmic rays enter the heliosphere, they interact with the solar wind and the HMF that modify their energy spectra. These modifications are directly related to solar activity and the total effect is called solar modulation. Solar activity varies strongly with time, rising from a minimum level when the Sun is quiet (with cosmic rays then having a maximum intensity at Earth) to a maximum period (when cosmic rays have

[21] Deceased.
[22] Now at School of Mathematics and Physics, China University of Geosciences, CN-430074 Wuhan, China.

a minimum intensity) and then returning to a new minimum to repeat the cycle. This solar cycle spans approximately 11 years. Solar activity modulates cosmic rays with the same cycle as a function of position in the heliosphere. Protons with rigidities up to at least 30 GV are affected and the effect becomes progressively larger as the rigidity decreases (e.g., Potgieter 2011). At each solar activity maximum the polarity of the solar magnetic field reverses. When the solar magnetic field lines point outward in the northern hemisphere and inward in the southern hemisphere, the Sun is said to be in an $A > 0$ cycle, whereas during an $A < 0$ cycle the solar magnetic field lines point inward (outward) in the northern (southern) hemisphere. Direct cosmic-ray measurements above a few MeV have been performed from the inner to the outer heliosphere (see, e.g., Heber & Potgieter 2006; Webber et al. 2012) and particularly at Earth where solar modulation effects are at their largest.

Understanding the origin and propagation of cosmic rays requires knowledge of the cosmic-ray energy spectra in the interstellar medium, i.e., uninfluenced by the Sun's magnetic field. These spectra, especially for protons, can be inferred from gamma-ray data (e.g., see Neronov et al. 2012). However, uncertainties are large and direct cosmic-ray measurements are preferable. *Voyager* space missions (Decker et al. 2005; Richardson et al. 2008) have passed the termination shock and may soon start sampling the cosmic radiation in the local interstellar medium. They will provide fundamental data to understand the basic features of the heliosphere. However, these cosmic-ray measurements are limited to the very low energy part of the spectra (from tens to a few 100 MeV), with galactic protons, helium, and oxygen strongly contaminated by the anomalous component (Stone et al. 2008). Higher energies are needed to fully address fundamental questions in cosmic-ray physics. Moreover, the energy spectra of rare components like antiparticles may yield indirect information regarding new physics such as dark matter. For example, the antiproton flux between a few hundred MeV and a few GeV can be used (e.g., Cerdeno et al. 2012; Asano et al. 2012; Garny et al. 2012) to constrain models with light (∼10 GeV) dark matter candidates put forward to interpret recent measurements by direct-detection experiments (Bernabei et al. 2000; Aalseth et al. 2011; Angloher et al. 2012). However, solar modulation has a relevant effect on the cosmic-ray spectra at these energies that needs to be disentangled to allow a comprehensive picture to emerge.

Precise measurements of cosmic-ray spectra over a wide rigidity range, from a few hundred MV to tens of GV over an extended period of time (covering a significant fraction of the solar cycle) can be used to study the effect of solar modulation in greater detail, including the convective and adiabatic cooling effect of the expanding solar wind and the diffusive and particle drift effects of the turbulent HMF. The most recent solar minimum activity period (2006–2009) and the consequent minimum modulation conditions for cosmic rays were unusual. It was expected that the new activity cycle would begin early in 2008. Instead, minimum modulation conditions continued until the end of 2009 when the highest levels of cosmic rays were recorded at Earth since the beginning of the space age (see, e.g., Mewaldt et al. 2010). This period of prolonged solar minimum activity is well suited to study the various modulation processes that affect the propagation of galactic cosmic rays inside the heliosphere.

PAMELA is a satellite-borne instrument designed for cosmic-ray antimatter studies. The instrument is flying on board the Russian *Resurs-DK1* satellite since 2006 June, in a semi-polar

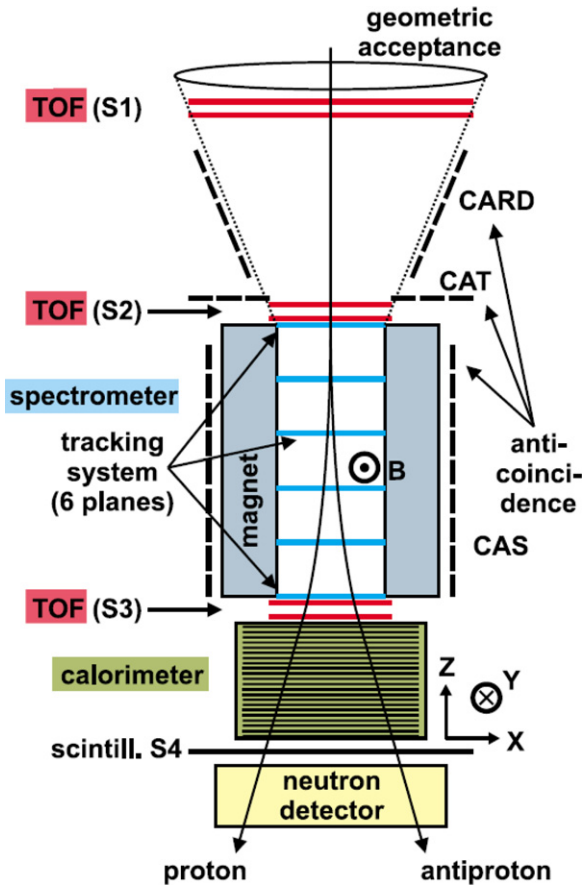

Figure 1. Schematic view of the PAMELA apparatus.
(A color version of this figure is available in the online journal.)

near-Earth orbit. PAMELA has provided important results on the antiproton (Adriani et al. 2009a) and positron (Adriani et al. 2009b) galactic abundances. The high-resolution magnetic spectrometer allowed hydrogen and helium spectral measurements up to 1.2 TV (Adriani et al. 2011), the highest limit ever achieved by this kind of experiment. We present here results on the long-term variations in the absolute flux of hydrogen nuclei, measured down to 400 MV.

The analysis, described in Section 3, is based on data collected between 2006 July and 2009 December. The analyzed period covers the unusually long most recent solar minimum. The large proton statistics collected by the instrument allowed the proton flux to be measured for each Carrington rotation[23] (hereafter the flux measured on this time basis will be referred as Carrington flux).

2. THE INSTRUMENT

The PAMELA instrument, shown schematically in Figure 1, comprises a number of highly redundant detectors, capable of identifying particles by providing charge (Ze), mass, rigidity ($R = pc/Ze$, with p momentum of the particle and c speed of light), and velocity (β) measurements over a very wide energy range. Multiple detectors are placed around a permanent magnet with a silicon micro-strip tracking system, providing charge and track deflection ($d = \pm 1/R$) information. A scintillator system (TOF: S1, S2, and S3) provides the trigger for event acquisition,

[23] Mean synodic rotational period of the Sun surface, corresponding to about 27.28 days (Carrington 1863).

the time-of-flight measurement, and further charge information. A silicon–tungsten calorimeter is used to perform hadron/lepton separation; a scintillator (S4) and a neutron detector placed at the bottom of the apparatus increase the rejection power at high energy. An anti-coincidence system (AC: CAS, CAT, and CARD) registers hits produced by particles entering from outside the instrument acceptance. A detailed description of the apparatus can be found in Picozza et al. (2007).

3. ANALYSIS

3.1. Event Selection

In order to give a valid trigger for data acquisition, a particle must cross the S2 and S3 scintillators, located above and below the tracking system, respectively. The requirement of a hit on S3 sets a limit on the minimum detectable rigidity, which for vertical protons is on average 400 MV, i.e., $\simeq$80 MeV of kinetic energy.

Clean events are selected by requiring a precision track in the spectrometer, a trajectory contained within the instrument acceptance, and no hits in the CARD and CAT scintillators. Protons are identified among all the selected particles by requiring a positive track curvature and ionization energy losses (dE/dX) in the tracking system consistent with a hydrogen nucleus. The dE/dX selection included deuterons, which in this work have been treated as being protons. Galactic particles have been selected by requiring that the measured rigidity was a factor 1.3 above the geomagnetic vertical cutoff, evaluated using the Störmer approximation, at a given orbital position. The satellite orbit has an inclination of 70°, which allows galactic particles to be studied down to the minimum detectable rigidity.

The analysis procedure was similar to previous work on high-energy proton and helium fluxes (Adriani et al. 2011). The major differences concern track-quality requirements and the fiducial volume definition. The procedure used in the proton and helium study aimed to maximize the spectrometer performance and minimize systematic uncertainties in the flux normalization, in order to perform a precise spectral measurement up to the highest achievable energy. The study presented in this paper aims to trace time variations in the low-energy particle flux, with the finest possible time binning. Hence, high-performing tracking was less important than high statistics. For this reason the tracking requirements were relaxed (at least three hits, instead of four, on both X and Y view, a track lever arm of at least four silicon planes in the tracker) and the fiducial volume was enlarged (bounded 1.5 mm from the magnet cavity walls, instead of 7 mm), allowing the collection of more particles with only a small degradation in the measurement precision in the energy range under study.

3.2. Flux Normalization

The absolute proton flux in the spectrometer was obtained by dividing the measured energy spectrum by the acquisition time, the geometrical acceptance, and the selection efficiency.

3.2.1. Acquisition Time

Flux evaluation was performed as a function of time, binning the data according to the Carrington rotations. The time period studied corresponds to Carrington rotation numbers 2045–2092. The acquisition time was evaluated for each energy bin as the total live time spent above the geomagnetic cutoff, outside the South Atlantic Anomaly and during periods when no solar events had occurred (hence 2006 December, when a large solar event took place, was excluded from the data). This work is based on data collected between 2006 July and 2009 December. The total live time was about 5×10^7 s ($\sim$590 days) above $\sim$20 GV, reducing to about 13% of this value at 0.4 GV, due to the relatively short time spent by the satellite at low geomagnetic locations. The accuracy of the live-time determination was cross-checked by comparing different clocks available in flight, which showed a relative difference of less than 0.2%.

3.2.2. Geometrical Factor

The geometrical factor for this analysis ($G = 19.9$ cm^2 sr) is determined by the requirement of containment within the fiducial volume: a reconstructed track had to be 1.5 mm away from the magnet walls and the TOF-scintillator edges. The geometrical factor is constant above 1 GV and slowly decreases by $\sim$2% to lower energies, where the curvature of the proton particle trajectory is no longer negligible.

The value of G has been evaluated with two independent numerical methods, which provided values consistent within 0.1%.

3.2.3. Selection Efficiency

The PAMELA instrument has been designed to provide redundant information on event topology and particle characteristics. This feature allowed the efficiencies of each detector to be measured directly from flight data. Due to the large proton statistics, detector behavior could be monitored over very short timescales. For this analysis, efficiencies were evaluated independently for each time interval, in order to follow any possible time variation of detector responses.

The major time-dependent effect was the sudden failure of some front-end chips in the tracking system. Chip failures started to occur few months after the launch of the satellite, initially with an almost constant rate. In the following years the rate of failures significantly decreased and the tracking system reached an almost stable condition near the end of 2009. The net effect was a progressive reduction of the tracking efficiency, since the number of hits available for track reconstruction decreased. No degradation in the signal-to-noise ratio and spatial resolution was observed.

The approach described in Adriani et al. (2011) for the evaluation of the tracking efficiency was used: a high energy average value was experimentally obtained using non-interacting minimum ionizing particles in the calorimeter from flight data and an energy-dependent correction factor was evaluated using Monte Carlo simulation. The average tracking efficiency was measured using a test sample of non-interacting relativistic protons in the imaging calorimeter. The resulting efficiency varied almost monotonically from $\simeq$94% during the first months to $\simeq$20% in the final months. The efficiency variation was correctly reproduced by the simulation, which included a map of dead channels as a function of time. Since the requirement of non-interacting minimum ionizing particles in the calorimeter selected essentially protons with rigidities $\geqslant$2 GV, the determination of the tracking efficiency at lower rigidities was performed using the simulation. The simulation results were normalized to experimental values at high rigidities after performing an identical selection. This was required because, due to the relatively poor tracking resolution of the calorimeter, the average efficiency values obtained using the calorimeter selection were different from the average efficiency of an isotropically distributed particle sample (as was the case for triggered events). This

normalization was applied to the simulation estimated efficiency that accounted for the full energy dependence of the tracking efficiency and was used for the flux estimation. When comparing the average experimental and simulated efficiencies, differences of less than 4% were found, except during the last few months of 2009 when the tracking efficiency fell below 40% and, consequently, the discrepancy became more significant, increasing up to 13%. These differences were included in the systematic uncertainties of the measurements. As a further check, two different simulation packages were used: GEANT3 (Brun et al. 1994) and GEANT4 (Agostinelli et al. 2003). The resulting efficiencies differed by $\simeq$1.5% and this was included in the systematic uncertainty.

TOF and AC selection efficiencies were evaluated relative to the tracking selection. For well-contained events, the TOF and AC responses were not correlated and the selection efficiencies could be measured independently. At low rigidities TOF and AC efficiency measurements were affected by background contamination in the test samples of low-energy secondary particles produced by high-energy primaries interacting with the apparatus. This contamination resulted in an underestimation of the efficiency, since background interactions were often associated with multiple hits in both the TOF and AC scintillators. An upper limit on this contamination was determined by excluding the TOF and AC conditions from the test sample selection, thereby adding background events into the test sample. The difference between the results was found to be $\simeq$6% in the lowest-energy bin. This value was conservatively treated as an asymmetric systematic uncertainty on the absolute flux.

3.3. Spectral Unfolding and Other Corrections

The proton spectrum measured in the spectrometer was corrected to the top of the payload by accounting for the effects of rigidity displacement due to finite spectrometer resolution and particle slow-down by ionization energy loss, the latter being more relevant at low energies. The correction was applied by means of an unfolding procedure, following the Bayesian approach proposed by D'Agostini (1995). The detector response matrix was obtained from the simulation. The resulting spectrum was corrected for the contamination of locally produced secondary particles and for attenuation due to particles interacting with the satellite and the instrument itself. In order to estimate the residual contamination of locally produced secondary particles, simulations of protons and helium nuclei isotropically hitting the PAMELA payload within a 2π solid angle were carried out. The estimated background was found to be less than 6% at 0.4 GV and inversely proportional to energy, becoming negligible above 1 GV. Flux attenuation, which was slightly energy dependent and amounted to 5%–6%, accounted for both particle loss by non-elastic interactions and loss and gain of particles from within the acceptance due to elastic scattering.

Finally, in order to correct for systematic time-dependent variations of the Carrington fluxes (see next section), these were normalized, at high energy (30–50 GeV), to the proton flux measured with the more stringent tracking conditions of Adriani et al. (2011) and averaged over the period 2006 July–2008 March.[24]

[24] An improved use of the simulation resulted in slightly higher selection efficiencies than previously estimated. Therefore, the proton spectrum of Adriani et al. (2011) should be lowered by 3.2%. Furthermore, the overall systematic uncertainty is slightly larger at low energies (4.5% at 1 GV).

3.4. Systematic Uncertainties

By relaxing the tracking selection the proton statistics could be significantly increased, allowing the proton flux to be evaluated on a Carrington rotation basis up to the end of 2009. This approach also led to an increase of the systematic uncertainties on the measured absolute fluxes.

The reliability of the flux determination was verified by studying the time variation of the flux at high energy (above 30 GeV) since no significant modulation effects are expected in this energy region. As a reference, we considered the fluxes obtained with the stringent tracking conditions and averaged over the period 2006 July–2008 March. Figure 2 shows the time dependence of the ratio between the Carrington fluxes and the reference flux for two high-energy intervals at about 30 GV and 47 GV. Two different selection criteria were considered: stringent (open circles; as in Adriani et al. 2011) and relaxed tracking selections (filled circles; this work).

Comparing the upper and lower panels of Figure 2 a correlation between the time profiles at different energies can be noticed, which indicates the presence of non-negligible systematic effects. The Carrington fluxes based on the analysis described in Adriani et al. (2011) fluctuate around a mean value consistent with the quoted $\simeq$4% systematic uncertainty, while the fluxes for this analysis show a decreasing trend, with a relative variation over the whole time interval of $\sim$10%. This time-dependent systematic effect was corrected as discussed in the previous section. The assumption behind this correction implies that PAMELA results are not sensitive to solar modulation-induced flux variations smaller than about 5%.

Further contributions to the total uncertainty resulted from the unfolding procedure (1%–5%) and from the correction to the top of the payload (1%).

4. RESULTS

Figure 3 shows the time profile of the proton flux for three energy intervals; the error bars are statistical, while the shaded area represents the quadratic sum of all systematic uncertainties. The systematic uncertainty is dominated by the tracking efficiency and reaches a minimum above a few tens of GeV and for the first Carrington rotations, when the tracking efficiency is maximum. Additional time- and energy-dependent contributions to the overall uncertainty have been introduced in order to account for both the reduced accuracy of the simulation in reproducing the spectrometer behavior as the detection efficiency decreases in time, and the larger uncertainty on the simulated efficiency at low energy.

Figure 4 shows the evolution of the Carrington proton energy spectra from 2006 July (blue curve) to 2009 December (red curve). Around 100 MeV proton intensities increased by $\simeq$20% over 12 months, from 2006 December to 2007 December, with a slightly larger increase of $\simeq$25% from 2007 December to 2008 December. For 2009, when solar minimum conditions continued to prevail throughout the heliosphere, intensities increased by almost 40%. From these data it is clear that protons (evident across the greater part of the energy spectrum) reached maximum intensities at the end of 2009.

5. DATA INTERPRETATION AND DISCUSSION

Figure 5 and Table 1 present the galactic proton spectra measured by PAMELA over four time periods. These data illustrate how the proton spectra evolved from late 2006 to late

Table 1
Hydrogen Flux Measured by PAMELA over Five Time Periods

Kinetic Energy (GeV)	Flux $(m^2\ s\ sr\ MeV)^{-1}$			
	2006 Nov 13–2006 Dec 4	2007 Nov 30–2007 Dec 27	2008 Nov 19–2008 Dec 15	2009 Dec 6–2010 Jan 1
0.082–0.095	$(0.721 \pm 0.032^{+0.061}_{-0.100})$	$(1.045 \pm 0.031^{+0.090}_{-0.102})$	$(1.191 \pm 0.035^{+0.105}_{-0.104})$	$(1.730 \pm 0.143^{+0.266}_{-0.163})$
0.095–0.10	$(0.759 \pm 0.036^{+0.063}_{-0.096})$	$(1.111 \pm 0.030^{+0.094}_{-0.098})$	$(1.332 \pm 0.034^{+0.116}_{-0.100})$	$(1.722 \pm 0.156^{+0.263}_{-0.160})$
0.10–0.11	$(0.818 \pm 0.030^{+0.067}_{-0.093})$	$(1.151 \pm 0.027^{+0.097}_{-0.094})$	$(1.401 \pm 0.031^{+0.121}_{-0.097})$	$(2.016 \pm 0.134^{+0.307}_{-0.158})$
0.11–0.12	$(0.893 \pm 0.034^{+0.072}_{-0.089})$	$(1.230 \pm 0.027^{+0.102}_{-0.091})$	$(1.477 \pm 0.031^{+0.126}_{-0.094})$	$(2.210 \pm 0.151^{+0.336}_{-0.157})$
0.12–0.13	$(0.928 \pm 0.030^{+0.074}_{-0.086})$	$(1.334 \pm 0.026^{+0.110}_{-0.088})$	$(1.543 \pm 0.029^{+0.131}_{-0.091})$	$(2.162 \pm 0.129^{+0.327}_{-0.155})$
0.13–0.15	$(0.960 \pm 0.028^{+0.076}_{-0.084})$	$(1.411 \pm 0.025^{+0.115}_{-0.086})$	$(1.607 \pm 0.027^{+0.135}_{-0.089})$	$(2.256 \pm 0.123^{+0.341}_{-0.154})$
0.15–0.16	$(1.030 \pm 0.028^{+0.081}_{-0.083})$	$(1.453 \pm 0.023^{+0.117}_{-0.085})$	$(1.675 \pm 0.026^{+0.139}_{-0.087})$	$(2.447 \pm 0.122^{+0.368}_{-0.153})$
0.16–0.17	$(1.085 \pm 0.027^{+0.084}_{-0.081})$	$(1.477 \pm 0.022^{+0.118}_{-0.083})$	$(1.727 \pm 0.025^{+0.142}_{-0.085})$	$(2.359 \pm 0.112^{+0.354}_{-0.152})$
0.17–0.19	$(1.123 \pm 0.025^{+0.086}_{-0.079})$	$(1.545 \pm 0.021^{+0.122}_{-0.081})$	$(1.805 \pm 0.024^{+0.147}_{-0.084})$	$(2.277 \pm 0.102^{+0.341}_{-0.151})$
0.19–0.21	$(1.164 \pm 0.024^{+0.088}_{-0.078})$	$(1.613 \pm 0.020^{+0.126}_{-0.080})$	$(1.865 \pm 0.023^{+0.150}_{-0.082})$	$(2.423 \pm 0.097^{+0.362}_{-0.150})$
0.21–0.22	$(1.194 \pm 0.022^{+0.090}_{-0.076})$	$(1.634 \pm 0.019^{+0.126}_{-0.078})$	$(1.899 \pm 0.021^{+0.152}_{-0.081})$	$(2.592 \pm 0.093^{+0.386}_{-0.149})$
0.22–0.24	$(1.222 \pm 0.022^{+0.091}_{-0.075})$	$(1.673 \pm 0.018^{+0.128}_{-0.077})$	$(1.968 \pm 0.021^{+0.156}_{-0.080})$	$(2.647 \pm 0.091^{+0.393}_{-0.149})$
0.24–0.26	$(1.278 \pm 0.021^{+0.094}_{-0.074})$	$(1.732 \pm 0.018^{+0.131}_{-0.076})$	$(2.031 \pm 0.020^{+0.159}_{-0.079})$	$(2.682 \pm 0.088^{+0.397}_{-0.148})$
0.26–0.29	$(1.359 \pm 0.020^{+0.098}_{-0.073})$	$(1.775 \pm 0.017^{+0.133}_{-0.075})$	$(2.047 \pm 0.019^{+0.159}_{-0.078})$	$(2.684 \pm 0.082^{+0.396}_{-0.148})$
0.29–0.31	$(1.371 \pm 0.020^{+0.098}_{-0.072})$	$(1.788 \pm 0.016^{+0.132}_{-0.074})$	$(2.025 \pm 0.018^{+0.155}_{-0.077})$	$(2.603 \pm 0.077^{+0.383}_{-0.147})$
0.31–0.34	$(1.380 \pm 0.019^{+0.098}_{-0.071})$	$(1.818 \pm 0.016^{+0.133}_{-0.073})$	$(2.040 \pm 0.017^{+0.155}_{-0.076})$	$(2.656 \pm 0.075^{+0.390}_{-0.147})$
0.34–0.36	$(1.381 \pm 0.018^{+0.097}_{-0.070})$	$(1.822 \pm 0.015^{+0.132}_{-0.072})$	$(2.036 \pm 0.017^{+0.153}_{-0.075})$	$(2.633 \pm 0.072^{+0.385}_{-0.146})$
0.36–0.39	$(1.398 \pm 0.017^{+0.097}_{-0.069})$	$(1.816 \pm 0.014^{+0.130}_{-0.072})$	$(2.019 \pm 0.016^{+0.150}_{-0.074})$	$(2.504 \pm 0.067^{+0.366}_{-0.146})$
0.39–0.43	$(1.410 \pm 0.016^{+0.096}_{-0.068})$	$(1.778 \pm 0.013^{+0.126}_{-0.071})$	$(1.983 \pm 0.015^{+0.146}_{-0.074})$	$(2.415 \pm 0.061^{+0.351}_{-0.146})$
0.43–0.46	$(1.396 \pm 0.016^{+0.094}_{-0.068})$	$(1.754 \pm 0.013^{+0.123}_{-0.070})$	$(1.959 \pm 0.014^{+0.143}_{-0.073})$	$(2.495 \pm 0.060^{+0.362}_{-0.145})$
0.46–0.50	$(1.391 \pm 0.015^{+0.093}_{-0.067})$	$(1.715 \pm 0.012^{+0.119}_{-0.069})$	$(1.941 \pm 0.014^{+0.140}_{-0.072})$	$(2.383 \pm 0.056^{+0.345}_{-0.145})$
0.50–0.54	$(1.349 \pm 0.014^{+0.089}_{-0.066})$	$(1.677 \pm 0.012^{+0.115}_{-0.068})$	$(1.844 \pm 0.013^{+0.132}_{-0.071})$	$(2.200 \pm 0.052^{+0.318}_{-0.144})$
0.54–0.58	$(1.328 \pm 0.014^{+0.086}_{-0.065})$	$(1.643 \pm 0.011^{+0.111}_{-0.068})$	$(1.789 \pm 0.012^{+0.126}_{-0.071})$	$(2.213 \pm 0.050^{+0.319}_{-0.144})$
0.58–0.62	$(1.300 \pm 0.009^{+0.084}_{-0.064})$	$(1.577 \pm 0.010^{+0.105}_{-0.067})$	$(1.731 \pm 0.013^{+0.121}_{-0.070})$	$(2.107 \pm 0.032^{+0.303}_{-0.144})$
0.62–0.67	$(1.254 \pm 0.008^{+0.080}_{-0.064})$	$(1.527 \pm 0.009^{+0.101}_{-0.066})$	$(1.641 \pm 0.012^{+0.114}_{-0.069})$	$(1.966 \pm 0.030^{+0.282}_{-0.143})$
0.67–0.72	$(1.220 \pm 0.008^{+0.077}_{-0.063})$	$(1.468 \pm 0.009^{+0.096}_{-0.065})$	$(1.587 \pm 0.011^{+0.109}_{-0.068})$	$(1.870 \pm 0.028^{+0.268}_{-0.143})$
0.72–0.77	$(1.173 \pm 0.007^{+0.073}_{-0.062})$	$(1.403 \pm 0.008^{+0.091}_{-0.065})$	$(1.510 \pm 0.011^{+0.102}_{-0.068})$	$(1.769 \pm 0.026^{+0.252}_{-0.143})$
0.77–0.83	$(1.125 \pm 0.007^{+0.069}_{-0.061})$	$(1.341 \pm 0.007^{+0.086}_{-0.064})$	$(1.431 \pm 0.010^{+0.096}_{-0.067})$	$(1.710 \pm 0.025^{+0.243}_{-0.142})$
0.83–0.89	$(1.064 \pm 0.006^{+0.064}_{-0.060})$	$(1.272 \pm 0.007^{+0.080}_{-0.063})$	$(1.357 \pm 0.009^{+0.090}_{-0.066})$	$(1.550 \pm 0.022^{+0.220}_{-0.142})$
0.89–0.96	$(1.003 \pm 0.006^{+0.060}_{-0.060})$	$(1.197 \pm 0.007^{+0.075}_{-0.062})$	$(1.273 \pm 0.009^{+0.084}_{-0.066})$	$(1.442 \pm 0.021^{+0.204}_{-0.142})$
0.96–1.02	$(0.964 \pm 0.005^{+0.057}_{-0.059})$	$(1.135 \pm 0.006^{+0.070}_{-0.062})$	$(1.192 \pm 0.008^{+0.077}_{-0.065})$	$(1.382 \pm 0.020^{+0.195}_{-0.141})$
1.02–1.09	$(0.919 \pm 0.005^{+0.053}_{-0.058})$	$(1.066 \pm 0.006^{+0.065}_{-0.061})$	$(1.127 \pm 0.007^{+0.072}_{-0.064})$	$(1.294 \pm 0.018^{+0.183}_{-0.141})$
1.09–1.17	$(0.860 \pm 0.005^{+0.049}_{-0.057})$	$(0.993 \pm 0.005^{+0.060}_{-0.060})$	$(1.041 \pm 0.007^{+0.066}_{-0.064})$	$(1.178 \pm 0.017^{+0.166}_{-0.141})$
1.17–1.25	$(0.813 \pm 0.004 \pm 0.046)$	$(0.934 \pm 0.005 \pm 0.056)$	$(0.983 \pm 0.006 \pm 0.062)$	$(1.105 \pm 0.016 \pm 0.155)$
1.25–1.34	$(0.753 \pm 0.004 \pm 0.042)$	$(0.860 \pm 0.005 \pm 0.051)$	$(0.903 \pm 0.006 \pm 0.056)$	$(1.030 \pm 0.014 \pm 0.144)$
1.34–1.42	$(0.708 \pm 0.004 \pm 0.039)$	$(0.813 \pm 0.004 \pm 0.047)$	$(0.845 \pm 0.006 \pm 0.052)$	$(0.931 \pm 0.013 \pm 0.130)$
1.42–1.52	$(0.650 \pm 0.004 \pm 0.035)$	$(0.748 \pm 0.004 \pm 0.043)$	$(0.782 \pm 0.005 \pm 0.048)$	$(0.862 \pm 0.012 \pm 0.120)$
1.52–1.62	$(0.607 \pm 0.003 \pm 0.033)$	$(0.693 \pm 0.004 \pm 0.039)$	$(0.719 \pm 0.005 \pm 0.044)$	$(0.789 \pm 0.011 \pm 0.110)$
1.62–1.72	$(0.562 \pm 0.003 \pm 0.030)$	$(0.640 \pm 0.003 \pm 0.036)$	$(0.670 \pm 0.004 \pm 0.040)$	$(0.720 \pm 0.010 \pm 0.100)$
1.72–1.83	$(0.520 \pm 0.003 \pm 0.027)$	$(0.590 \pm 0.003 \pm 0.033)$	$(0.612 \pm 0.004 \pm 0.036)$	$(0.675 \pm 0.010 \pm 0.094)$
1.83–1.95	$(0.481 \pm 0.003 \pm 0.025)$	$(0.540 \pm 0.003 \pm 0.030)$	$(0.562 \pm 0.004 \pm 0.033)$	$(0.605 \pm 0.009 \pm 0.084)$
1.95–2.07	$(0.441 \pm 0.002 \pm 0.023)$	$(0.501 \pm 0.003 \pm 0.027)$	$(0.512 \pm 0.004 \pm 0.030)$	$(0.547 \pm 0.008 \pm 0.076)$
2.07–2.20	$(0.412 \pm 0.002 \pm 0.021)$	$(0.450 \pm 0.002 \pm 0.024)$	$(0.461 \pm 0.003 \pm 0.027)$	$(0.499 \pm 0.008 \pm 0.069)$
2.20–2.33	$(0.374 \pm 0.002 \pm 0.019)$	$(0.409 \pm 0.002 \pm 0.022)$	$(0.428 \pm 0.003 \pm 0.024)$	$(0.450 \pm 0.007 \pm 0.062)$
2.33–2.48	$(0.347 \pm 0.002 \pm 0.017)$	$(0.377 \pm 0.002 \pm 0.020)$	$(0.388 \pm 0.003 \pm 0.022)$	$(0.411 \pm 0.006 \pm 0.057)$
2.48–2.62	$(0.315 \pm 0.002 \pm 0.015)$	$(0.348 \pm 0.002 \pm 0.018)$	$(0.356 \pm 0.003 \pm 0.020)$	$(0.390 \pm 0.006 \pm 0.054)$
2.62–2.78	$(0.286 \pm 0.002 \pm 0.014)$	$(0.318 \pm 0.002 \pm 0.016)$	$(0.322 \pm 0.002 \pm 0.018)$	$(0.334 \pm 0.005 \pm 0.046)$
2.78–2.94	$(0.262 \pm 0.002 \pm 0.012)$	$(0.288 \pm 0.002 \pm 0.015)$	$(0.291 \pm 0.002 \pm 0.016)$	$(0.303 \pm 0.005 \pm 0.042)$
2.94–3.12	$(0.239 \pm 0.001 \pm 0.011)$	$(0.258 \pm 0.002 \pm 0.013)$	$(0.262 \pm 0.002 \pm 0.014)$	$(0.276 \pm 0.005 \pm 0.038)$
3.12–3.30	$(0.215 \pm 0.001 \pm 0.010)$	$(0.234 \pm 0.001 \pm 0.012)$	$(0.239 \pm 0.002 \pm 0.013)$	$(0.251 \pm 0.004 \pm 0.034)$
3.30–3.49	$(0.195 \pm 0.001 \pm 0.009)$	$(0.210 \pm 0.001 \pm 0.010)$	$(0.215 \pm 0.002 \pm 0.012)$	$(0.223 \pm 0.004 \pm 0.031)$

Table 1
(Continued)

Kinetic Energy (GeV)	Flux $(m^2\ s\ sr\ MeV)^{-1}$			
	2006 Nov 13–2006 Dec 4	2007 Nov 30–2007 Dec 27	2008 Nov 19–2008 Dec 15	2009 Dec 6–2010 Jan 1
3.49–3.69	$(0.175 \pm 0.001 \pm 0.008)$	$(0.189 \pm 0.001 \pm 0.009)$	$(0.194 \pm 0.002 \pm 0.010)$	$(0.204 \pm 0.004 \pm 0.028)$
3.69–4.12	$(151.4 \pm 0.7 \pm 6.9) \times 10^{-3}$	$(163.3 \pm 0.7565 \pm 8.050) \times 10^{-3}$	$(164.7 \pm 0.9853 \pm 8.790) \times 10^{-3}$	$(0.172 \pm 0.002 \pm 0.023)$
4.12–4.59	$(124.4 \pm 0.6 \pm 5.6) \times 10^{-3}$	$(132.0 \pm 0.6391 \pm 6.446) \times 10^{-3}$	$(134.3 \pm 0.8364 \pm 7.113) \times 10^{-3}$	$(0.141 \pm 0.002 \pm 0.019)$
4.59–5.11	$(99.15 \pm 0.5 \pm 4.4) \times 10^{-3}$	$(106.8 \pm 0.5402 \pm 5.168) \times 10^{-3}$	$(109.1 \pm 0.7083 \pm 5.731) \times 10^{-3}$	$(0.113 \pm 0.002 \pm 0.015)$
5.11–5.68	$(81.38 \pm 0.4 \pm 3.6) \times 10^{-3}$	$(85.34 \pm 0.4537 \pm 4.093) \times 10^{-3}$	$(86.97 \pm 0.5944 \pm 4.536) \times 10^{-3}$	$(0.091 \pm 0.001 \pm 0.012)$
5.68–6.30	$(65.27 \pm 0.4 \pm 2.9) \times 10^{-3}$	$(68.61 \pm 0.3820 \pm 3.262) \times 10^{-3}$	$(69.55 \pm 0.4994 \pm 3.601) \times 10^{-3}$	$(0.069 \pm 0.001 \pm 0.009)$
6.30–6.99	$(52.12 \pm 0.3 \pm 2.3) \times 10^{-3}$	$(54.86 \pm 0.3211 \pm 2.587) \times 10^{-3}$	$(55.60 \pm 0.4197 \pm 2.859) \times 10^{-3}$	$(56.69 \pm 0.9533 \pm 7.693) \times 10^{-3}$
6.99–7.74	$(41.66 \pm 0.3 \pm 1.8) \times 10^{-3}$	$(43.65 \pm 0.2691 \pm 2.042) \times 10^{-3}$	$(44.15 \pm 0.3514 \pm 2.255) \times 10^{-3}$	$(44.91 \pm 0.7967 \pm 6.088) \times 10^{-3}$
7.74–8.57	$(33.18 \pm 0.2 \pm 1.4) \times 10^{-3}$	$(34.31 \pm 0.2241 \pm 1.593) \times 10^{-3}$	$(34.65 \pm 0.2923 \pm 1.759) \times 10^{-3}$	$(34.70 \pm 0.6572 \pm 4.700) \times 10^{-3}$
8.57–9.48	$(26.26 \pm 0.2 \pm 1.1) \times 10^{-3}$	$(26.80 \pm 0.1856 \pm 1.235) \times 10^{-3}$	$(27.12 \pm 0.2424 \pm 1.368) \times 10^{-3}$	$(27.44 \pm 0.5473 \pm 3.713) \times 10^{-3}$
9.48–10.48	$(208.8 \pm 1.5 \pm 8.8) \times 10^{-4}$	$(214.3 \pm 1.556 \pm 9.872) \times 10^{-4}$	$(21.32 \pm 0.2014 \pm 1.075) \times 10^{-3}$	$(21.77 \pm 0.4564 \pm 2.945) \times 10^{-3}$
10.48–11.57	$(164.0 \pm 1.2 \pm 6.9) \times 10^{-4}$	$(167.1 \pm 1.286 \pm 7.697) \times 10^{-4}$	$(167.7 \pm 1.672 \pm 8.456) \times 10^{-4}$	$(16.86 \pm 0.3755 \pm 2.281) \times 10^{-3}$
11.57–12.77	$(128.9 \pm 1.0 \pm 5.5) \times 10^{-4}$	$(130.2 \pm 1.061 \pm 5.998) \times 10^{-4}$	$(134.6 \pm 1.399 \pm 6.785) \times 10^{-4}$	$(13.03 \pm 0.3083 \pm 1.763) \times 10^{-3}$
12.77–14.09	$(100.1 \pm 0.8 \pm 4.2) \times 10^{-4}$	$(103.4 \pm 0.8845 \pm 4.762) \times 10^{-4}$	$(102.8 \pm 1.143 \pm 5.182) \times 10^{-4}$	$(10.22 \pm 0.2554 \pm 1.384) \times 10^{-3}$
14.09–15.54	$(78.59 \pm 0.7 \pm 3.3) \times 10^{-4}$	$(79.72 \pm 0.7250 \pm 3.672) \times 10^{-4}$	$(78.55 \pm 0.9319 \pm 3.960) \times 10^{-4}$	$(8.339 \pm 0.2150 \pm 1.129) \times 10^{-3}$
15.54–17.12	$(62.71 \pm 0.6 \pm 2.7) \times 10^{-4}$	$(64.08 \pm 0.6064 \pm 2.952) \times 10^{-4}$	$(62.57 \pm 0.7736 \pm 3.154) \times 10^{-4}$	$(62.71 \pm 1.735 \pm 8.486) \times 10^{-4}$
17.12–18.86	$(47.92 \pm 0.5 \pm 2.0) \times 10^{-4}$	$(49.08 \pm 0.4937 \pm 2.261) \times 10^{-4}$	$(49.15 \pm 0.6357 \pm 2.478) \times 10^{-4}$	$(47.39 \pm 1.400 \pm 6.413) \times 10^{-4}$
18.86–20.76	$(37.16 \pm 0.4 \pm 1.6) \times 10^{-4}$	$(37.96 \pm 0.4066 \pm 1.748) \times 10^{-4}$	$(38.06 \pm 0.5230 \pm 1.919) \times 10^{-4}$	$(38.42 \pm 1.181 \pm 5.200) \times 10^{-4}$
20.76–22.85	$(28.92 \pm 0.3 \pm 1.2) \times 10^{-4}$	$(29.32 \pm 0.3398 \pm 1.351) \times 10^{-4}$	$(28.47 \pm 0.4282 \pm 1.435) \times 10^{-4}$	$(28.76 \pm 9.688 \pm 3.892) \times 10^{-4}$
22.85–25.15	$(225.8 \pm 2.6 \pm 9.6) \times 10^{-5}$	$(23.07 \pm 0.2879 \pm 1.063) \times 10^{-4}$	$(22.61 \pm 0.3642 \pm 1.140) \times 10^{-4}$	$(21.59 \pm 0.8009 \pm 2.922) \times 10^{-4}$
25.15–27.66	$(171.3 \pm 2.2 \pm 7.2) \times 10^{-5}$	$(173.8 \pm 2.389 \pm 8.006) \times 10^{-5}$	$(173.5 \pm 3.049 \pm 8.745) \times 10^{-5}$	$(18.35 \pm 0.7055 \pm 2.484) \times 10^{-4}$
27.66–30.42	$(138.0 \pm 1.9 \pm 5.8) \times 10^{-5}$	$(137.7 \pm 2.031 \pm 6.344) \times 10^{-5}$	$(138.8 \pm 2.603 \pm 6.997) \times 10^{-5}$	$(14.03 \pm 0.5883 \pm 1.898) \times 10^{-4}$
30.42–33.44	$(103.8 \pm 1.5 \pm 4.4) \times 10^{-5}$	$(105.6 \pm 1.699 \pm 4.862) \times 10^{-5}$	$(101.5 \pm 2.127 \pm 5.118) \times 10^{-5}$	$(10.95 \pm 0.4965 \pm 1.482) \times 10^{-4}$
33.44–36.75	$(81.42 \pm 1.3 \pm 3.4) \times 10^{-5}$	$(80.24 \pm 1.416 \pm 3.696) \times 10^{-5}$	$(81.51 \pm 1.820 \pm 4.109) \times 10^{-5}$	$(76.20 \pm 0.3955 \pm 1.031) \times 10^{-4}$
36.75–40.39	$(63.41 \pm 1.1 \pm 2.7) \times 10^{-5}$	$(62.97 \pm 1.199 \pm 2.900) \times 10^{-5}$	$(62.22 \pm 1.520 \pm 3.137) \times 10^{-5}$	$(61.51 \pm 3.396 \pm 8.323) \times 10^{-5}$
40.39–44.37	$(47.29 \pm 0.9 \pm 2.0) \times 10^{-5}$	$(49.30 \pm 1.014 \pm 2.271) \times 10^{-5}$	$(49.86 \pm 1.300 \pm 2.514) \times 10^{-5}$	$(47.38 \pm 2.847 \pm 6.412) \times 10^{-5}$
44.37–48.74	$(35.22 \pm 0.8 \pm 1.5) \times 10^{-5}$	$(33.67 \pm 0.801 \pm 1.551) \times 10^{-5}$	$(35.50 \pm 1.049 \pm 1.790) \times 10^{-5}$	$(36.99 \pm 2.404 \pm 5.006) \times 10^{-5}$

Note. The first and second errors represent the statistical and systematic uncertainties, respectively.

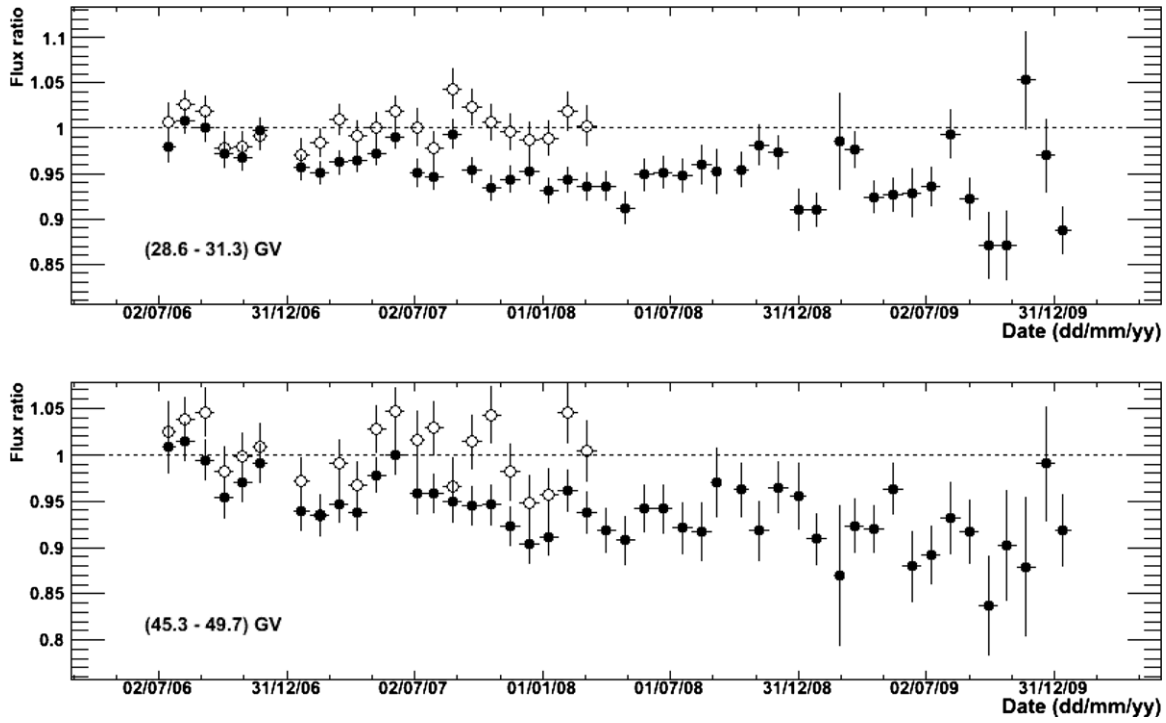

Figure 2. Carrington proton fluxes shown relative to the flux obtained in Adriani et al. (2011; value averaged over the period 2006 July–2008 March) for stringent tracking criteria (open circles) and relaxed tracking criteria (filled circles). Two energy intervals are presented.

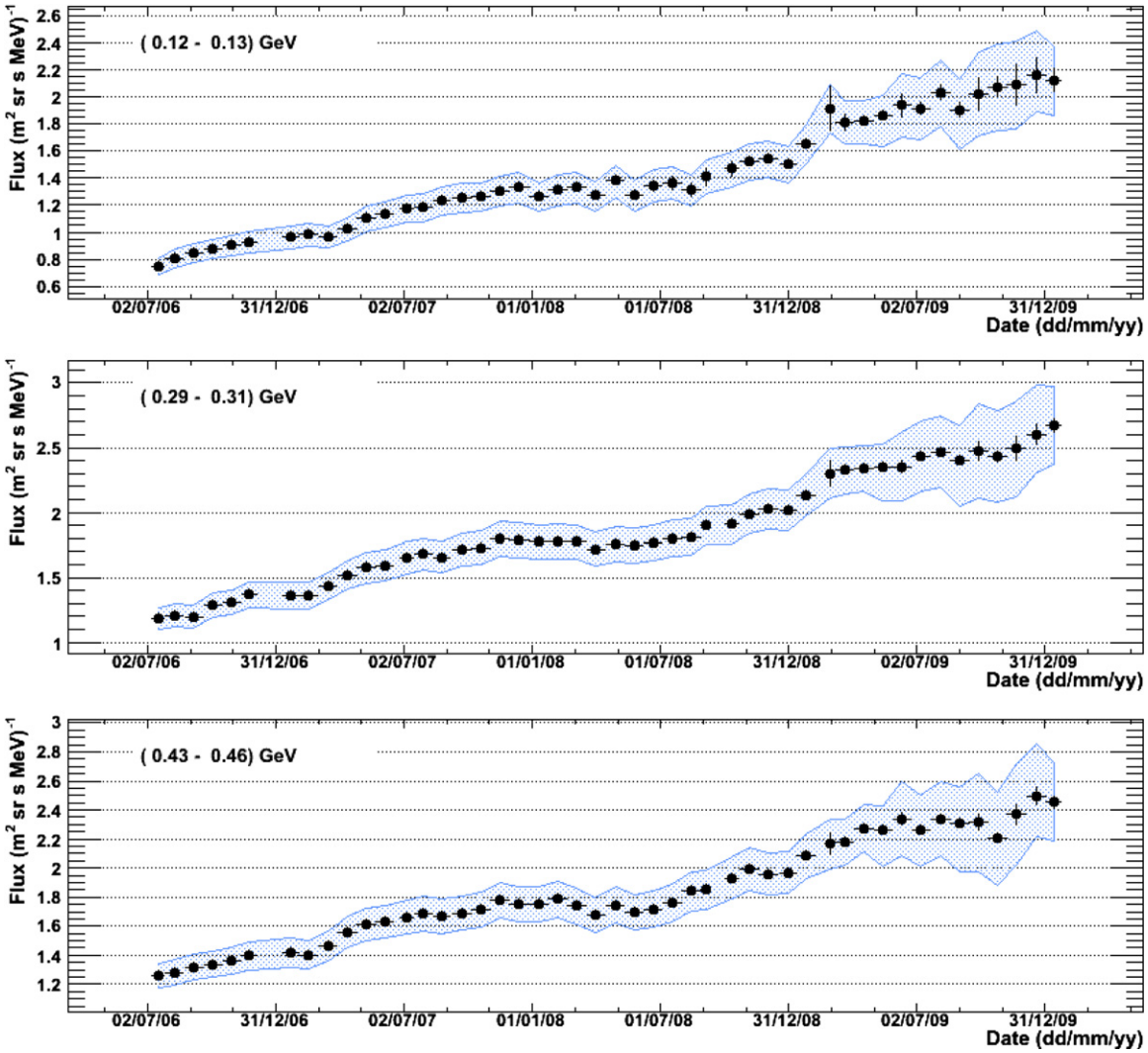

Figure 3. Time profile of the proton flux for three energy intervals (from top to bottom): 0.597–0.625 GeV, 0.99–1.04 GeV, and 2.99–3.13 GeV. The error bars are statistical and the shaded area represents the quadratic sum of all systematic uncertainties.

(A color version of this figure is available in the online journal.)

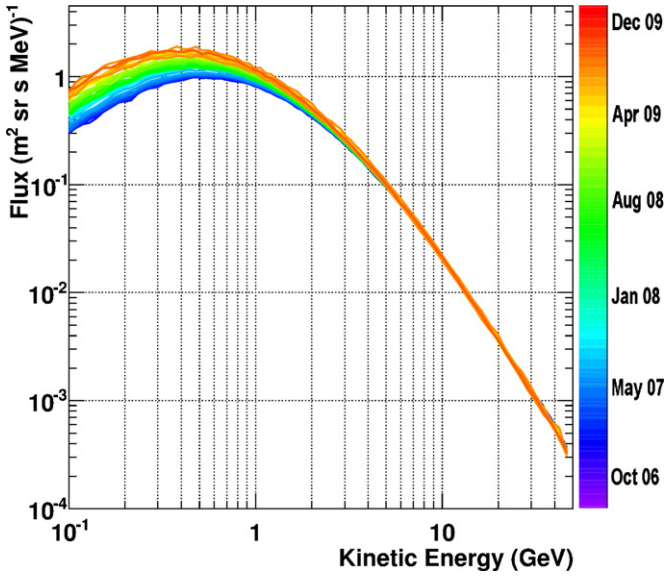

Figure 4. Evolution of the proton energy spectrum as particle intensities approached the period of minimum solar activity, from 2006 July (violet) to 2009 December (red). The region between the blue and red curves indicates the spread in proton fluxes during this time.

(A color version of this figure is available in the online journal.)

2009. The latter represents the highest proton flux observed by PAMELA. In Figure 5 the PAMELA proton spectra are overlaid with the corresponding computed spectra (solid lines). A full three-dimensional (3D) model was used to compute the differential intensity of cosmic-ray protons at Earth from 10 MeV to 30 GeV. The model is based on the numerical solution of the Parker transport equation (Parker 1965), including all four major modulation mechanisms: convection, particle drift caused by gradients and curvatures in the HMF, diffusion described by a full 3D diffusion tensor, and adiabatic energy changes. For these calculations, a local interstellar spectrum (LIS) was assumed (shown as a solid black line in Figure 5). The proton LIS was based on that by Langner & Potgieter (2004) modified at high energies to match PAMELA observations. It follows from the comparison between the model and observations that the proton spectra became progressively softer, as expected, from 2006 but requiring larger diffusion coefficients at lower energies than anticipated. At the same time full particle drifts occurred but with the modulation drift effects somewhat obscured by the effective diffusion. This caused the effect of the HMF wavy current sheet to be less well correlated to increases in cosmic-ray intensities at Earth. Details concerning the modulation model and theoretical assumptions and implications will be published in a subsequent paper (Potgieter et al. 2013).

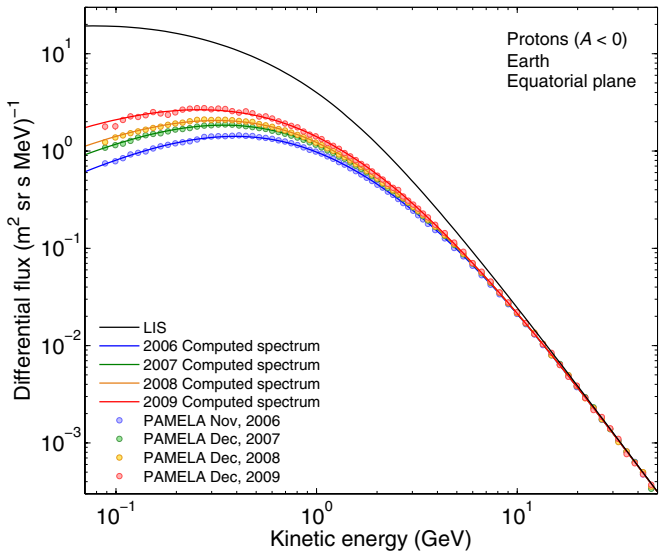

Figure 5. PAMELA proton spectra for 2006 November (blue), 2007 December (green), 2008 December (yellow), and 2009 December (red) overlaid with the corresponding computed spectra (solid lines; Potgieter et al. 2013). The LIS used for the computation is also shown (black solid line).

(A color version of this figure is available in the online journal.)

We acknowledge support from The Italian Space Agency (ASI), Deutsches Zentrum für Luft- und Raumfahrt (DLR), The Swedish National Space Board, The Swedish Research Council, The Russian Space Agency (Roscosmos), and The Russian Foundation for Basic Research. Partial financial support was given by the South African National Research Council (NRF) for the numerical modeling.

REFERENCES

Aalseth, C. E., Barbeau, P. S., Bowden, N. S., et al. 2011, PhRvL, 106, 131301
Adriani, O., Barbarino, G. C., Bazilevskaya, G. A., et al. 2009a, PhRvL, 102, 051101
Adriani, O., Barbarino, G. C., Bazilevskaya, G. A., et al. 2009b, Natur, 458, 607
Adriani, O., Barbarino, G. C., Bazilevskaya, G. A., et al. 2011, Sci, 332, 69
Agostinelli, S., Allison, J., Amako, K., et al. 2003, NIMPA, 506, 250
Angloher, G., Bauer, M., Bavykina, I., et al. 2012, EPJC, 72, 1971
Asano, M., Bringmann, T., & Weniger, C. 2012, PhLB, 709, 128
Bernabei, R., Belli, P., Cerulli, R., et al. 2000, PhLB, 480, 23
Brun, R., Carminati, F., & Giani, S. 1994, GEANT, Detector Description and Simulation Tool, CERN-W5013 (Geneva: CERN)
Carrington, R. C. 1863, Observations of the Spots on the Sun from November 9, 1853 to March 24, 1861, Made at Redhill (London: Williams and Norgate)
Cerdeno, D. G., Delahaye, T., & Lavalle, J. 2012, NuPhB, 854, 738
D'Agostini, G. 1995, NIMPA, 362, 487
Decker, R. B., Krimigis, S. M., Roelof, E. C., et al. 2005, Sci, 309, 2020
Garny, M., Ibarra, A., & Vogl, S. 2012, JCAP, 4, 033
Heber, B., & Potgieter, M. S. 2006, SSRv, 127, 117
Langner, U. W., & Potgieter, M. S. 2004, JGR, 109, A01103
Mewaldt, R. A., Davis, A. J., Lave, K. A., et al. 2010, ApJL, 723, L1
Neronov, A., Semikoz, D. V., & Taylor, A. M. 2012, PhRvL, 108, 051105
Parker, E. N. 1965, P&SS, 13, 9
Picozza, P., Galper, A. M., Castellini, G., et al. 2007, APh, 27, 296
Potgieter, M. S. 2011, SSRv, DOI:10.1007/s11214-011-9750-7
Potgieter, M. S., Vos, E. E., Boezio, M., et al. 2013, ApJ, submitted (arXiv:1302.1284)
Richardson, J. D., Kasper, J. C., Wang, C., Belcher, J. W., & Lazarus, A. J. 2008, Natur, 454, 63
Stone, E. C., Cummings, A. C., McDonald, F. B., et al. 2008, Natur, 454, 71
Webber, W. R., McDonald, F. B., Cummings, A. C., et al. 2012, GeoRL, 39, L06107